Journal of Magnetic Resonance **148,** 388–397 (2001)
doi:10.1006/jmre.2000.2261, available online at http://www.idealibrary.com on IDEAL®

The Effect of Spin Relaxation on ENDOR Spectra Recorded at High Magnetic Fields and Low Temperatures

B. Epel,*[,1] A. Pöppl,† P. Manikandan,* S. Vega,* and D. Goldfarb*

*Department of Chemical Physics, Weizmann Institute of Science, Rehovot 76100, Israel; and †Facultät für Physik and Geowissenschaften, Universität Leipzig, Linnestrasse 5, D-04103 Leipzig, Germany

Received August 31, 2000; revised November 13, 2000

A simple theoretical model that describes the pulsed Davies electron-nuclear double resonance (ENDOR) experiment for an electron spin $S = \frac{1}{2}$ coupled to a nuclear spin $I = \frac{1}{2}$ was developed to account for unusual W-band (95 GHz) ENDOR effects observed at low temperatures. This model takes into account the thermal polarization along with all internal relaxation processes in a four-level system represented by the electron- and nuclear-spin relaxation times T_{1e} and T_{1n}, respectively, and the cross-relaxation time, T_{1x}. It is shown that under conditions of sufficiently high thermal spin polarization, nuclei can exhibit asymmetric ENDOR spectra in two cases: the first when $t_{mix} \gg T_{1e}$ and T_{1n}, $T_{1x} \gg T_{1e}$, where ENDOR signals from the α manifold are negative and those of the β manifold positive, and the second when the cross- and/or nuclear-relaxation times are longer than the repetition time ($t_{mix} \ll T_{1e} \ll t_R$ and T_{1n}, $T_{1x} > t_R$). In that case the polarization of the ENDOR signals becomes opposite to the previous case, the lines in the α manifolds are positive, and those of the β manifold are negative. This case is more likely to be encountered experimentally because it does not require a very long mixing time and is a consequence of the saturation of the nuclear transitions. Using this model the experimental t_{mix} and t_R dependencies of the W-band ^{1}H ENDOR amplitudes of [Cu(imidazole)$_4$]Cl$_2$ were reproduced and the values of T_{1e} and $T_{1x} \gg T_{1e}$ were determined. The presence of asymmetry in the ENDOR spectrum is useful as it directly provides the sign of the hyperfine coupling. The presented model allows the experimentalist to adjust experimental parameters, such as t_{mix} and t_R, in order to optimize the desired appearance of the spectrum.

Key Words: **high field; pulsed EPR; ENDOR; spin–lattice relaxation.**

INTRODUCTION

Electron-nuclear double resonance (ENDOR) spectroscopy is one of the most useful methods for measuring the NMR frequencies of nuclei in paramagnetic systems, which in turn provide the hyperfine and nuclear quadrupole interactions. One of the standard ways for recording ENDOR spectra is the application of the pulsed Davies ENDOR experiment (*1*), shown in Fig. 1. The spectrum is obtained by measuring the echo amplitude as a function of the frequency of the radiofrequency (RF) pulse. This experiment can be divided into three periods, (i) the preparation stage, which consists of the selective inversion of one of the EPR transitions by a microwave (MW) π-pulse, (ii) the mixing period, which starts with the RF pulse that inverts selectively one of the NMR transitions and is followed by a time, t_{mix}, during which relaxation processes can take place, and (iii) the detection period, which consists of an echo detection sequence applied at the same frequency as the preparation pulse. ENDOR measurements carried out at high fields ($B_0 > 2.4$ T and $\nu > 70$ GHz) and low temperatures exhibit relatively high S/N due to the large thermal electron polarization. This large thermal polarization may, however, under certain experimental conditions, also lead to unusual ENDOR effects. Recently, a number of high-field ENDOR studies, which employed relatively long RF pulses, reported the appearance of negative ENDOR effects at low temperatures (*2, 3*). Bennebroek and Schmidt (*4*) attributed this effect to high thermal polarization in combination with an electron spin–lattice relaxation time, T_{1e}, that is shorter than the total mixing time. In the case of an electron spin $S = \frac{1}{2}$ coupled to a nuclear spin, this results in a negative ENDOR effect for lines belonging to the $M_S = -\frac{1}{2}$ manifold and a positive one for lines in the $M_S = \frac{1}{2}$ manifold. Thus, the asymmetry between the manifolds provides a mean to determine the sign of the hyperfine coupling.

We have also observed asymmetric ENDOR effects in a number of W-band (95 GHz) ^{1}H ENDOR spectra. But unlike the conditions mentioned above, these asymmetries were obtained during Davies ENDOR experiments with $t_{mix} \ll T_{1e}$ (*5*). In addition, the difference between the ENDOR effects for $M_S = \frac{1}{2}$ and $M_S = -\frac{1}{2}$ was found to be t_{mix} dependent. To explain these results it is thus necessary to extend the work of Bennebroek and Schmidt (*4*) and to consider all possible relaxation pathways during the ENDOR experiment. The possibility that the differences in ENDOR line intensities arise from the hyperfine enhancement factor (*6*) is excluded because for weakly coupled protons at W-band this factor is negligibly small.

[1] On leave from MRS Laboratory, Kazan State University, Kazan, 420008, Russia.

1090-7807/01 $35.00

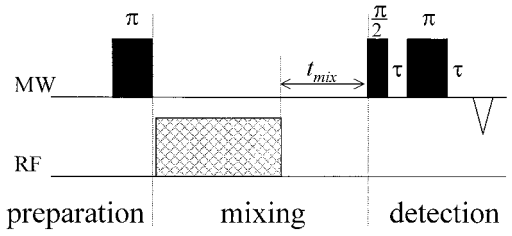

FIG. 1. The pulse sequences of the Davies ENDOR experiment.

In this publication we present a general theoretical model for the evaluation of the magnitudes of ENDOR lines in the Davies ENDOR experiment in the presence of relaxation. This model is based on a four-level system composed of an electron spin $S = \frac{1}{2}$ coupled to one nucleus $I = \frac{1}{2}$. All possible relaxation pathways, including the electron and nuclear spin–lattice relaxation, and cross-relaxation times, T_{1e}, T_{1n}, T_{1x}, respectively, as well as the temperature and the frequency of EPR transition, are taken into account. In the following it will be shown, both theoretically and experimentally, that the asymmetric intensities of the ^{1}H ENDOR doublets for $t_{mix} \ll T_{1e}$ occurs when $T_{1e} \ll t_R < T_{1n}$, T_{1x}. Namely, it is a consequence of insufficiently long repetition time, t_R. Under these conditions the spin system does not fully relax to equilibrium prior to the application of the next ENDOR sequence in a multiple accumulation experiment. We will also show that this effect is not exclusive to high fields and that, in principle, it can also be observed at low temperatures during X- and Q-band experiments. The validity of the theoretical model is demonstrated by the analysis of the W-band ENDOR effect of the copper tetra-imidazole complex in a frozen solution.

THEORY

Let us consider an ensemble of independent equivalent four-level systems consisting of an electron spin, $S = \frac{1}{2}$, coupled to a nuclear spin $I = \frac{1}{2}$ with a constant total population that is normalized to unity. The energy levels are labeled by numbers from 1 to 4, according to Fig. 2, and their populations are n_{1-4}, respectively. At thermal equilibrium the populations follow the Boltzmann distribution.

The Hamiltonian describing this system contains the electronic and nuclear Zeeman interactions and in addition a hyperfine coupling term. The first order ENDOR frequencies, ν_α and ν_β, corresponding to the transitions in the α ($M_S = \frac{1}{2}$) and β ($M_S = -\frac{1}{2}$) manifolds, are given (*7*):

$$\nu_\alpha = \left| -\nu_N + \frac{a}{2} \right|, \quad \nu_\beta = \left| -\nu_N - \frac{a}{2} \right|, \qquad [1]$$

For clarity, in the following we shall assume that $a > 0$ and $a < 2\nu_N$, where ν_N is the nuclear Larmor frequency. This, nevertheless, does not reduce the generality of our model, which is applicable for any sign and value of a. Under the above conditions, the ENDOR spectrum will consist of a doublet, centered at ν_N with a splitting of a. The low-frequency ENDOR line will correspond to an NMR transition in the α manifold with frequency $\nu_\alpha = \nu_{24}$, while the high-frequency line corresponds to a transition in the β manifold with $\nu_\beta = \nu_{13}$. The frequencies of the allowed EPR transitions are ν_{12} and ν_{34} and those of the forbidden EPR transitions and ν_{14} and ν_{23}. Three types of relaxation rates define the process of thermal equilibration (see Fig. 2): (i) The electron-spin relaxation rates $\Gamma_\uparrow$ and $\Gamma_\downarrow$ (with $\Delta M_S = 1$, $\Delta m = 0$), the nuclear-spin relaxation rate Γ_n (with $\Delta M_S = 0$, $\Delta m = 1$), and the cross-relaxation rates $\Gamma^{14}_{x\uparrow}$, $\Gamma^{14}_{x\downarrow}$ and $\Gamma^{23}_{x\uparrow}$, $\Gamma^{23}_{x\downarrow}$ (with $\Delta M_S = 1$, $\Delta m = \pm 1$).

The ENDOR experiment is best described using the full spin-density matrix formalism (see, i.e., Gemperle and Schweiger (*6*)). However, since in the ideal Davies ENDOR experiment it is sufficient to consider only the populations of the energy levels, the off-diagonal elements of the density matrix can be ignored and we can restrict our calculations to the diagonal elements only. This is further justified by the fact that any nuclear or electron coherences that may be generated during the experiment will decay in a time significantly shorter than any other relevant time interval of the experiment.

The populations of the four levels can be described in a form of a vector $\mathbf{n} = \{n_1, n_2, n_3, n_4\}$ and its time evolution during any time interval between MW or RF pulses of an ENDOR experiment can be represented by the master equation (*8*)

$$\frac{d\mathbf{n}}{dt} = -\Gamma\mathbf{n}. \qquad [2]$$

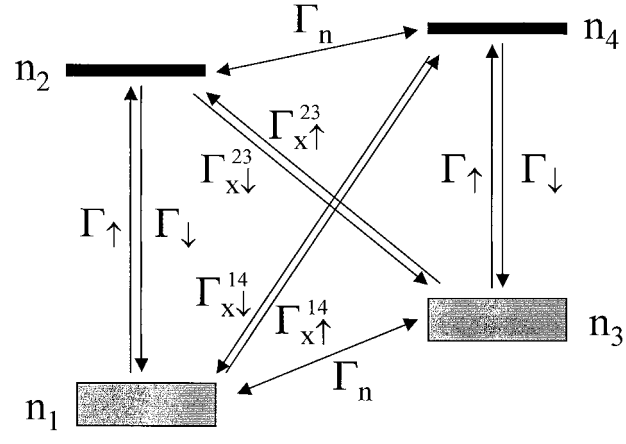

FIG. 2. A schematic illustration of the four-level system, $S = \frac{1}{2}$, $I = \frac{1}{2}$, and the corresponding relaxation rates. The thickness of the levels represents relative populations.

Γ is a relaxation matrix,

$$\Gamma = \begin{pmatrix} \Gamma_\uparrow + \Gamma_n + \Gamma_{x\uparrow}^{14} & -\Gamma_\downarrow & -\Gamma_n & -\Gamma_{x\downarrow}^{14} \\ -\Gamma_\uparrow & \Gamma_\downarrow + \Gamma_n + \Gamma_{x\downarrow}^{23} & -\Gamma_{x\uparrow}^{23} & -\Gamma_n \\ -\Gamma_n & -\Gamma_{x\downarrow}^{23} & \Gamma_\uparrow + \Gamma_n + \Gamma_{x\uparrow}^{23} & -\Gamma_\downarrow \\ -\Gamma_{x\uparrow}^{14} & -\Gamma_n & -\Gamma_\uparrow & \Gamma_\downarrow + \Gamma_n + \Gamma_{x\downarrow}^{14} \end{pmatrix}, \quad [3]$$

which represents the relaxation process towards thermal equilibrium. To obtain the Boltzmann distribution of the population as the solution of Eq. [2] in thermal equilibrium, the ratio between the "up" and "down" relaxation rates must be equal to (*9*)

$$\frac{\Gamma_\uparrow}{\Gamma_\downarrow} = \frac{\Gamma_{x\uparrow}^{14}}{\Gamma_{x\downarrow}^{14}} = \frac{\Gamma_{x\uparrow}^{23}}{\Gamma_{x\downarrow}^{23}} = \exp\left(-\frac{h\nu}{kT}\right). \quad [4]$$

Here we assumed that at thermal equilibrium the populations of the states with the same M_S (1–3 and 2–4) are equal and populations of states with different M_S differ by the Boltzmann factor; h and k are the Plank and Boltzmann constants, respectively, $\nu \approx \nu_{12} \approx \nu_{34}$ is the EPR transition frequency, and T is the temperature. Equation [4] is justified because the nuclear-spin Zeeman interaction and the hyperfine coupling constant are much smaller than the electron-spin Zeeman interaction. Similarly, we assume that $\Gamma_{x\uparrow}^{14} = \Gamma_{x\uparrow}^{23} = \Gamma_{x\uparrow}$, $\Gamma_{x\downarrow}^{14} = \Gamma_{x\downarrow}^{23} = \Gamma_{x\downarrow}$ and Eq. [4] becomes

$$\frac{\Gamma_\uparrow}{\Gamma_\downarrow} = \frac{\Gamma_{x\uparrow}}{\Gamma_{x\downarrow}} = \exp\left(-\frac{h\nu}{kT}\right). \quad [5]$$

The validity of Eq. [5] can be checked by solving the master equation at thermal equilibrium, namely, $d\mathbf{n}/dt = 0$. The solution of Eq. [2] is then

$$\mathbf{n}^B = \frac{1}{2(\Gamma_\downarrow + \Gamma_\uparrow + \Gamma_{1x\uparrow} + \Gamma_{1x\downarrow})} \begin{pmatrix} \Gamma_\downarrow + \Gamma_{x\downarrow} \\ \Gamma_\uparrow + \Gamma_{x\uparrow} \\ \Gamma_\downarrow + \Gamma_{x\downarrow} \\ \Gamma_\uparrow + \Gamma_{x\uparrow} \end{pmatrix}, \quad [6]$$

where $\mathbf{n}^B$ is given by the Boltzmann distribution. As long as the equilibrium state populations obey $n_1 = n_3$ and $n_2 = n_4$, $\mathbf{n}^B$ is independent of Γ_n, and according to Eq. [5],

$$\frac{n_2^B}{n_1^B} = \frac{n_4^B}{n_3^B} = \frac{\Gamma_\uparrow + \Gamma_{x\uparrow}}{\Gamma_\downarrow + \Gamma_{x\downarrow}} = \frac{\Gamma_\uparrow}{\Gamma_\downarrow} = \frac{\Gamma_{x\uparrow}}{\Gamma_{x\downarrow}} = \exp\left(-\frac{h\nu}{kT}\right) \quad [7]$$

is obtained. The n_i^B's in Eq. [7] are the components of $\mathbf{n}^B$.

The general solution of Eq. [2] is

$$\mathbf{n}(t) = e^{-\Gamma t}\mathbf{n}(0), \quad [8]$$

where $\mathbf{n}(0)$ denotes an initial state. The eigenvalues of Γ define the characteristic relaxation rates of the system, which correspond to the relaxation parameters measured in an experiment. In the Appendix we present the explicit expressions of the eigenvalues of Γ for two cases, $\Gamma_x = 0$ and $\Gamma_n = 0$. In most cases the major relaxation rates depend on the sum of the "up" and "down" relaxation rates. Therefore, for further comparison between experimental and theoretical results, the relaxation times are defined as

$$T_{1e} = \frac{1}{\Gamma_\uparrow + \Gamma_\downarrow}, \quad T_{1n} = \frac{1}{2\Gamma_n}, \quad T_{1x} = \frac{1}{\Gamma_{x\uparrow} + \Gamma_{x\downarrow}}. \quad [9]$$

To describe the evolution of the population of the energy levels during the ENDOR experiment we introduce operators that represent the selective MW and RF inversion pulses. These are

$$P_I^{12} = \begin{pmatrix} 0 & 1 & 0 & 0 \\ 1 & 0 & 0 & 0 \\ 0 & 0 & 1 & 0 \\ 0 & 0 & 0 & 1 \end{pmatrix}, \quad P_I^{34} = \begin{pmatrix} 1 & 0 & 0 & 0 \\ 0 & 1 & 0 & 0 \\ 0 & 0 & 0 & 1 \\ 0 & 0 & 1 & 0 \end{pmatrix}$$

$$P_{RF}^{\alpha} = \begin{pmatrix} 0 & 0 & 1 & 0 \\ 0 & 1 & 0 & 0 \\ 1 & 0 & 0 & 0 \\ 0 & 0 & 0 & 1 \end{pmatrix}, \quad P_{RF}^{\beta} = \begin{pmatrix} 1 & 0 & 0 & 0 \\ 0 & 0 & 0 & 1 \\ 0 & 0 & 1 & 0 \\ 0 & 1 & 0 & 0 \end{pmatrix}, \quad [10]$$

where P_I^{12} and P_I^{34} invert the 1–2 and 3–4 EPR transitions and P_{RF}^{α} and P_{RF}^{β} the 1–3 and 2–4 NMR transitions at frequencies ν_α and ν_β, respectively. The effect of the echo detection sequence on the populations can be represented by the nonunitary matrices P_D^{12} and P_D^{34},

$$P_D^{12} = \begin{pmatrix} \frac{1}{2} & \frac{1}{2} & 0 & 0 \\ \frac{1}{2} & \frac{1}{2} & 0 & 0 \\ 0 & 0 & 1 & 0 \\ 0 & 0 & 0 & 1 \end{pmatrix}, \quad P_D^{34} = \begin{pmatrix} 1 & 0 & 0 & 0 \\ 0 & 1 & 0 & 0 \\ 0 & 0 & \frac{1}{2} & \frac{1}{2} \\ 0 & 0 & \frac{1}{2} & \frac{1}{2} \end{pmatrix}. \quad [11]$$

The population vector just before the application of the echo detection sequence can be readily calculated using the above operators. When no RF is applied, or when its frequency is far off-resonance, the population is

$$\mathbf{n}(t_{\mathrm{mix}}) = e^{-\Gamma t_{\mathrm{mix}}} P_{\mathrm{I}}^{12} \mathbf{n}(0), \qquad [12]$$

where $\mathbf{n}(0)$ represents the population at the beginning of the ENDOR experiment. The echo signal at the end of each experiment is proportional to

$$I_{\mathrm{echo}} = n_1(t_{\mathrm{mix}}) - n_2(t_{\mathrm{mix}}). \qquad [13]$$

This value corresponds to the baseline (background) of the ENDOR spectrum. When the RF pulse is applied on-resonance, at ν_α or ν_β, the populations before the echo detection are

$$\mathbf{n}(t_{\mathrm{mix}}) = e^{-\Gamma t_{\mathrm{mix}}} P_{\mathrm{RF}}^{\alpha} P_{\mathrm{I}}^{12} \mathbf{n}(0), \qquad [14]$$

$$\mathbf{n}(t_{\mathrm{mix}}) = e^{-\Gamma t_{\mathrm{mix}}} P_{\mathrm{RF}}^{\beta} P_{\mathrm{I}}^{12} \mathbf{n}(0). \qquad [15]$$

In general, the initial states $\mathbf{n}(0)$ in Eqs. [12, 14, 15] can differ from each other and need not be the Boltzmann state, $\mathbf{n}^{\mathrm{B}}$. In a typical Davies ENDOR measurement the EPR echo amplitude is obtained by signal averaging. At each RF frequency the ENDOR experiment is repeated with a repetition time, t_{R}, and the echo amplitudes are accumulated. When t_{R} is much longer than any of the relaxation times in the system, the initial state $\mathbf{n}(0)$ for each experiment is equal to the Boltzmann state $\mathbf{n}^{\mathrm{B}}$. However, when t_{R} is not sufficiently long, the initial states are changing during the accumulation. Assuming that the initial states converges fast to the respective steady state limits, $\mathbf{n}_0$, $\mathbf{n}_0^{\alpha}$, and $\mathbf{n}_0^{\beta}$, it is possible to substitute $\mathbf{n}(0)$ in Eqs. [12, 14, 15] with these limits, which in turn can be determined by solving the following equations:

$$(e^{-\Gamma(t_{\mathrm{R}}-t_{\mathrm{mix}})} P_{\mathrm{D}}^{12} e^{-\Gamma t_{\mathrm{mix}}} P_{\mathrm{I}}^{12}) \mathbf{n}_0 = \mathbf{n}_0, \qquad [16]$$

$$(e^{-\Gamma(t_{\mathrm{R}}-t_{\mathrm{mix}})} P_{\mathrm{D}}^{12} e^{-\Gamma t_{\mathrm{mix}}} P_{\mathrm{RF}}^{\alpha} P_{\mathrm{I}}^{12}) \mathbf{n}_0^{\alpha} = \mathbf{n}_0^{\alpha}, \qquad [17]$$

$$(e^{-\Gamma(t_{\mathrm{R}}-t_{\mathrm{mix}})} P_{\mathrm{D}}^{12} e^{-\Gamma t_{\mathrm{mix}}} P_{\mathrm{RF}}^{\beta} P_{\mathrm{I}}^{12}) \mathbf{n}_0^{\beta} = \mathbf{n}_0^{\beta}. \qquad [18]$$

Equation [16] corresponds to the case that no RF is applied, whereas Eqs. [17] and [18] correspond to cases where the RF is applied at ν_α or ν_β, respectively.

We define an ENDOR efficiency parameter, F_{ENDOR}, as

$$F_{\mathrm{ENDOR}} = \frac{I_{\mathrm{echo}}^{\mathrm{on}}(t_{\mathrm{mix}}, t_{\mathrm{R}}) - I_{\mathrm{echo}}^{\mathrm{off}}(t_{\mathrm{mix}}, t_{\mathrm{R}})}{2I_{\mathrm{echo}}^{0}}, \qquad [19]$$

where the echo amplitudes $I_{\mathrm{echo}}^{\mathrm{off}}(t_{\mathrm{mix}}, t_{\mathrm{R}})$ and $I_{\mathrm{echo}}^{\mathrm{on}}(t_{\mathrm{mix}}, t_{\mathrm{R}})$ are the ENDOR signals obtained in the absence and presence of a RF pulse on-resonance with an NMR transition, respectively. I_{echo}^{0} in the denominator is the echo amplitude after a single two-pulse EPR echo experiment with the same τ as that used in the ENDOR experiment and $t_{\mathrm{R}} \gg T_{1\mathrm{e}}, T_{1\mathrm{n}}, T_{1\mathrm{x}}$. I_{echo}^{0} provides the normalization factor that is independent of t_{R} and t_{mix} (the echo amplitudes are obtained from Eq. [13]). For long t_{R} and t_{mix}, when the spin system has relaxed to thermal equilibrium

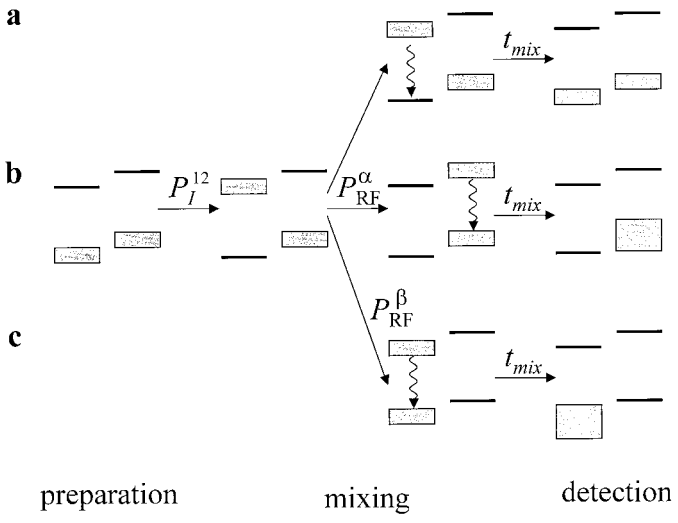

FIG. 3. A schematic illustration of the behavior of population distribution of the four-level system during an ENDOR sequence in presence of electron-spin relaxation. (a) The time evolution in the absence of an RF pulse. (b, c) The time evolution with an RF pulse applied in α and β manifolds, respectively. The wiggly arrows represent electron-spin relaxation.

before the detection sequence, $F_{\mathrm{ENDOR}} = 0$, whereas $F_{\mathrm{ENDOR}} = 0.5$ when the detection sequence is applied immediately after the RF inversion pulse ($t_{\mathrm{mix}} \ll T_{1\mathrm{e}}, T_{1\mathrm{n}}, T_{1\mathrm{x}}$).

The evolution of the populations described by Eqs. [12–15] and the steady state solutions derived from Eqs. [16–18] are determined by six independent parameters: three relaxation times ($T_{1\mathrm{e}}$, $T_{1\mathrm{n}}$, T_{x}), the two time delays of the ENDOR sequence (t_{mix}, t_{R}), and the polarization vector at thermal equilibrium ($\mathbf{n}^{\mathrm{B}}$), defined by the temperature and the frequency of the EPR transition. In the following we will evaluate the ENDOR efficiency for different values of these parameters. To simplify the analysis we will assume that $T_{1\mathrm{e}} \ll t_{\mathrm{R}}$, namely that the repetition time of the signal accumulation experiment is much longer than the electron spin–lattice relaxation time. This situation is typical for most experimental conditions under which ENDOR spectra are measured.

First we will discuss some limiting cases which lead to asymmetric ENDOR spectra.

$T_{1x} = \infty$, $T_{1e} \ll T_{1n} \ll t_R$

Figure 3 shows the evolution of the population distribution during a Davies ENDOR experiment in the limiting case of $T_{1\mathrm{n}} \gg t_{\mathrm{mix}}$. Because $T_{1\mathrm{n}} \ll t_{\mathrm{R}}$, the system returns to the thermal equilibrium after each ENDOR measurement, and the population vector at the beginning of the next experiment is equal to $\mathbf{n}^{\mathrm{B}}$. The evolution of the populations in the absence of RF pulse is shown in Fig. 3a, whereas Figs. 3b and 3c represent the evolution for on-resonance RF pulses at ν_α or ν_β, respectively. In the first case, immediately after the selective MW pulse, P_{I}^{12}, the populations of the 1–2 transition are inverted and those of 3–4 remain unchanged. During the mixing time the electronic

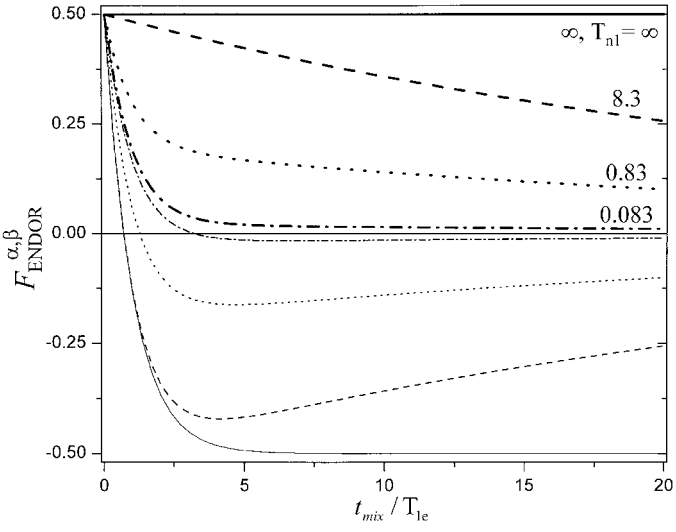

FIG. 4. The dependence of $F^{\alpha,\beta}_{\mathrm{ENDOR}}$ on t_{mix} at different temperatures. The $h\nu/kT$ ratios are indicated in the figure. Thin lines correspond to $F^{\alpha}_{\mathrm{ENDOR}}$ and thick lines to $F^{\beta}_{\mathrm{ENDOR}}$. The solid line corresponds to $h\nu/kT = \infty$, $t_{\mathrm{R}} = \infty$, $T_{1x} = \infty$, and $T_{1n} = \infty$. In all other cases $T_{1n}/T_{1e} = 30$, $t_{\mathrm{R}} = \infty$, $T_{1x} = \infty$.

relaxation brings the system back to thermal equilibrium. The echo detection sequence monitors the population difference of the 1–2 transition and $I^{\mathrm{off}}_{\mathrm{echo}}(t_{\mathrm{mix}})$ starts from $-I^{0}_{\mathrm{echo}}$ at $t_{\mathrm{mix}} = 0$ and grows toward I^{0}_{echo} at larger t_{mix}. In the second and third cases the populations after the RF pulse are redistributed such that at $t_{\mathrm{mix}} = 0$ levels 1–2 and 3–4 are equally populated. If at this position in time the echo signal is measured, both $I^{\alpha}_{\mathrm{echo}}(0)$ and $I^{\beta}_{\mathrm{echo}}(0)$ would be zero and $F^{\alpha}_{\mathrm{ENDOR}}(0) = F^{\beta}_{\mathrm{ENDOR}}(0) = 0.5$. For t_{mix} longer than T_{1e}, where $T_{1n} = \infty$, the electron-spin relaxation transfers the whole population to the 1 or 3 states, depending on the RF frequency. In this case the echo signals, $I^{\alpha}_{\mathrm{echo}}(t_{\mathrm{mix}})$ and $I^{\beta}_{\mathrm{echo}}(t_{\mathrm{mix}})$, both start at 0 and become 0 and $2I^{0}_{\mathrm{echo}}$, respectively with increasing t_{mix}. The value of $F^{\alpha\beta}_{\mathrm{ENDOR}}$ starts at 0.5 for both manifolds and evolves toward $F^{\alpha}_{\mathrm{ENDOR}}(t_{\mathrm{mix}}) = -0.5$ and $F^{\beta}_{\mathrm{ENDOR}}(t_{\mathrm{mix}}) = 0.5$. This yields for $t_{\mathrm{mix}} > T_{1e}$ an asymmetric ENDOR spectrum with a negative amplitude at ν_{α} and a positive amplitude at ν_{β}, as described earlier by Bennebroek and Schmidt (*4*).

When T_{1n} is of the same order of t_{mix} the absolute values of $F^{\alpha,\beta}_{\mathrm{ENDOR}}(t_{\mathrm{mix}})$ decrease with increasing t_{mix} and become dependent on the Boltzmann factor. The lower the temperatures, the longer it takes for the populations to reach equilibrium (for the same T_{1e} and T_{1n}). Figure 4 depicts the dependence of $F^{\alpha,\beta}_{\mathrm{ENDOR}}$ on t_{mix} for $T_{1n}/T_{1e} = 30$ and for three Boltzmann factors, $h\nu/kT = 8.3$, 0.83, and 0.083. The value 0.83 corresponds to $\nu = 95$ GHz (W-band) and a temperature of 5.5 K and the other values to 10 times higher and lower frequencies, or 10 times lower and higher temperatures. These plots show that at 5.5 K, $F^{\alpha}_{\mathrm{ENDOR}}$ and $F^{\beta}_{\mathrm{ENDOR}}$ have opposite signs at long mixing times even at X-band frequencies. Thus, spectral asymmetry is expected to be observed if S/N permits.

$T_{1x} = \infty$, $T_{1n} > t_R$

Up to this point t_{R} was assumed to be longer than any relaxation time and therefore each single ENDOR experiment started with a spin system in thermal equilibrium and a Boltzmann distribution of the populations. However, when t_{R} becomes of the order of T_{1n}, the $F^{\alpha,\beta}_{\mathrm{ENDOR}}$ values become dependent on t_{R}. In this case the steady state populations $\mathbf{n}_0$, $\mathbf{n}^{\alpha}_0$, and $\mathbf{n}^{\beta}_0$ must be evaluated from Eqs. [16–18], and then used to calculate the echo amplitudes and the ENDOR efficiencies.

When $t_{\mathrm{mix}} \gg T_{1e}$ the distribution of populations after the mixing stage is almost identical to those described previously. However, for $t_{\mathrm{mix}} < T_{1e}$ the behavior is completely different. Figure 5 illustrates the evolution of the populations in this case during the second accumulation in the ENDOR experiment with $T_{1n} = T_{1x} = \infty$. It demonstrates that in the absence of an RF pulse the system reaches thermal equilibrium after t_{R} and $I^{\mathrm{off}}_{\mathrm{echo}}$ equals $-I^{0}_{\mathrm{echo}}$ (Fig. 5a). When an RF pulse is applied at ν_{α}, the ENDOR sequence does not affect the populations of the monitored EPR transition, and as in the case of "normal" ENDOR, $I^{\alpha}_{\mathrm{echo}}$ becomes 0 (Fig. 5b). In contrast, when the RF pulse affects the β transition, the whole population is gathered at level 2, resulting in a negative echo amplitude $I^{\mathrm{off}}_{\mathrm{echo}} = -2I^{0}_{\mathrm{echo}}$ (Fig. 5c). Thus, for short t_{mix}, as usually employed in standard experimental conditions, $F^{\alpha}_{\mathrm{ENDOR}} = 0.5$ and $F^{\beta}_{\mathrm{ENDOR}} = -0.5$.

Figures 3 and 5 suggest that under the condition $T_{1n} = T_{1x} = \infty$ a steady state is reached for the initial populations already after the first experiment. Simulations have shown that for common relaxation times the number of repetitions needed to reach this state is not more than 3.

The dependence of $F^{\alpha,\beta}_{\mathrm{ENDOR}}$ on t_{mix} for $t_{\mathrm{R}}/T_{1e} = 10$ and

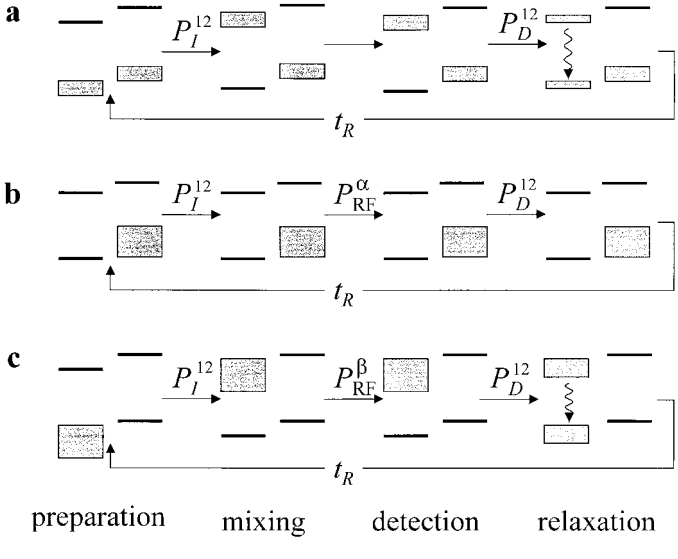

FIG. 5. A schematic illustration of the behavior of population distribution during the second shot in ENDOR sequence in the presence of electron-spin relaxation for $T_{1x} = \infty$, $T_{1n} > t_{\mathrm{R}}$. (a) The time evolution in the absence of RF pulse. (b, c) The time evolution with RF pulse applied in α and β manifolds, respectively. The wiggly arrows represent electron-spin relaxation.

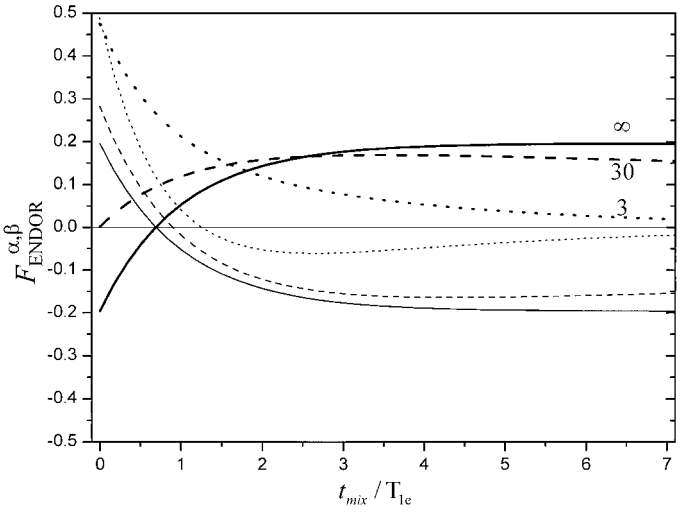

FIG. 6. Simulations of the dependence of $F^{\alpha,\beta}_{\rm ENDOR}$ on $t_{\rm mix}$ for different T_{1n}/T_{1e} values which are indicated in the figure. Thin lines correspond to $F^{\alpha}_{\rm ENDOR}$ and thick lines to $F^{\beta}_{\rm ENDOR}$. In all cases $t_R/T_{1e} = 10$ and $h\nu/kT = 0.83$.

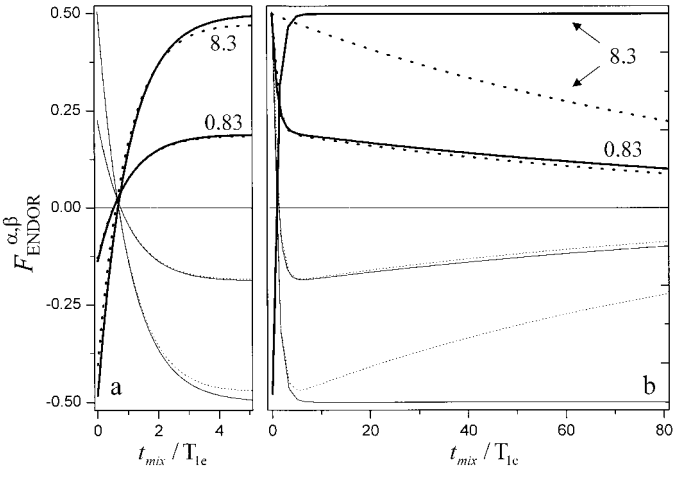

FIG. 7. The dependence of $F^{\alpha,\beta}_{\rm ENDOR}$ on $t_{\rm mix}$, for different values of $h\nu/kT$ and t_R/T_{1e}. The $h\nu/kT$ values are indicated in the figure. The solid line corresponds to $T_{1x}/T_{1e} = 100$, $T_{1n} = \infty$. Dotted line corresponds to $T_{1n}/T_{1e} = 100$, $T_x = \infty$. Thin lines correspond to $F^{\alpha}_{\rm ENDOR}$ and thick lines to $F^{\beta}_{\rm ENDOR}$. In (a) $t_R/T_{1e} = 10$ and in (b) $t_R/T_{1e} = 1000$.

different values of T_{1n}/T_{1e} is shown in Fig. 6. As T_{1n}/T_{1e} decreases, $F^{\beta}_{\rm ENDOR}$ (0) increases and approaches the value of $F^{\alpha}_{\rm ENDOR}$ (0). In contrast, when $t_{\rm mix} \gg T_{1e}$ the relation $F^{\alpha}_{\rm ENDOR} = -F^{\beta}_{\rm ENDOR}$ is almost independent of T_{1n}/T_{1e}.

$T_{1n} = \infty$, $T_{1x} \neq \infty$

Figure 7 (left) shows that the dependence of $F^{\alpha,\beta}_{\rm ENDOR}$ on T_{1x} at relatively high temperatures and small t_R is similar to the dependence on T_{1n}. It is, however, possible to differentiate between these two relaxation mechanisms. The nuclear relaxation equilibrates the populations of levels 1 and 3 with a process that is independent of temperature. In the absence of nuclear relaxation these populations can reach thermal equilibrium due to a complex process characterized by a relaxation time that increases for decreasing temperature (see Appendix). A comparison of the dependences of $F^{\alpha,\beta}_{\rm ENDOR}$ on $t_{\rm mix}$ at $h\nu/kT = 8.3$ for systems with nuclear relaxation and without cross-relaxation and vice versa is presented in Fig. 7 (right). Even at $h\nu/kT = 0.83$ the coefficient $\exp(-h\nu/kT)$ leads to a substantial decrease of the cross-relaxation efficiency. This is demonstrated in Fig. 8, where the dependences of $F^{\alpha,\beta}_{\rm ENDOR}$ on t_R is presented for equal nuclear and cross-relaxation rates. These plots also show that the optimal repetition rate for ENDOR experiments is determined by T_{1n} (or T_{1x}) and may be much longer than T_{1e}. A more explicit description of the different effects of the nuclear- and cross-relaxation is given in the Appendix.

EXPERIMENTAL

Sample Preparation

An aqueous solution of a copper tetra-imidazole complex, $[Cu(Imid)_4]^{2+}$ (Cu-Imid) was prepared as reported in the literature (*10*). The Cu(II) concentration of the sample used in all experiments was 2 mM in H_2O/glycerol (1:1 vol/vol).

Spectroscopic Measurements

Pulsed Davies ENDOR measurements were performed at W-band (94.9 GHz) on a homebuilt spectrometer (*11*) at 5.5 K. All reported experiments were carried out with MW $\pi/2$ and π pulses of 0.1 and 0.2 μs, respectively, and with an echo delay time, τ, of 0.35 μs. The duration of the RF π-pulses was 14 μs, as determined from the Rabi oscillations of selected ENDOR

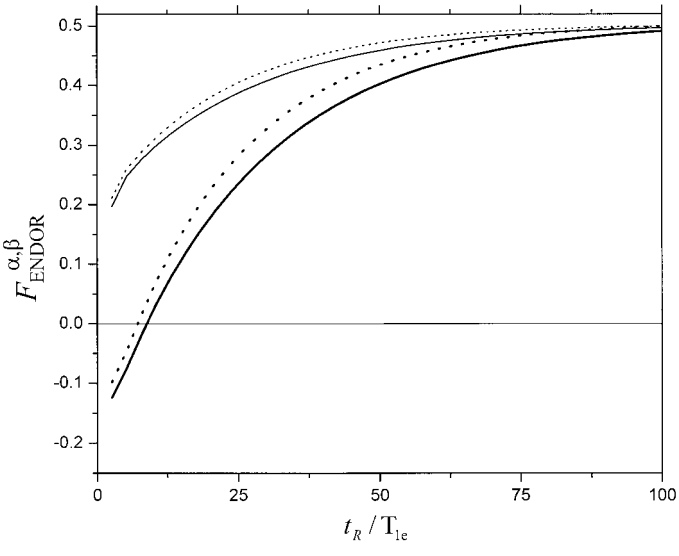

FIG. 8. The dependence of $F^{\alpha,\beta}_{\rm ENDOR}$ on t_R for $h\nu/kT = 0.83$ and $t_{\rm mix} = 6$ μs. Solid lines correspond to $T_{1x}/T_{1e} = 22$, $T_{1n} = \infty$, dotted lines correspond to $T_{1n}/T_{1e} = 22$ and $T_{1x} = \infty$. Thin lines correspond to $F^{\alpha}_{\rm ENDOR}$ and thick lines to $F^{\beta}_{\rm ENDOR}$.

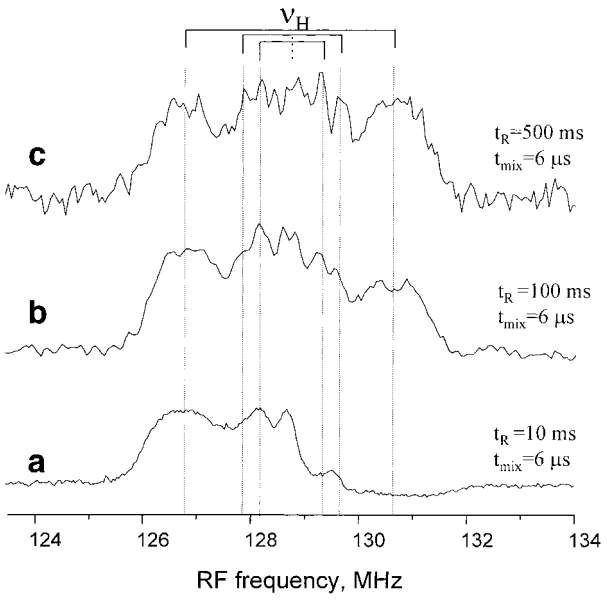

FIG. 9. ENDOR spectra of Cu-Imid recorded at 5.5 K and different experimental parameters as listed in the figure. The position of the ^{1}H Larmor frequency, ν_H, is marked. The vertical lines represent the positions of the various doublets. The number of accumulations for each frequency points are 30 (a), 10 (b), and 3 (c).

transitions in the Cu-Imid spectrum. All spectra were obtained after 3–30 accumulations. Field-sweep echo-detected (FS-ED) EPR spectra were recorded using the two-pulse echo sequence, where the echo amplitude is measured as a function of the magnetic field.

RESULTS

The W-band FS-ED EPR spectrum of Cu-Imid in a frozen solution features a powder pattern typical for an axial g-tensor, where the ^{63,65}Cu hyperfine splitting is not resolved. The W-band ^{1}H Davies ENDOR spectrum recorded at a magnetic field of 3.02 T, which is near $g_\parallel$, and with our standard experimental conditions, $T = 5.5$ K, $t_R = 10$ ms, and $t_{mix} = 6$ μs, is shown in Fig. 9a. The spectrum is highly asymmetric and consists of three major doublets. The first exhibits broad inhomogeneous lines at 126.8 and 130.6 MHz, corresponding to a hyperfine coupling constant, a_a, of 3.8 MHz, assigned to one type of protons, labeled H_a. The second doublet, at 127.9 and 129.6 MHz with $a_b = 1.1$ MHz is due to H_b protons, and the third one at 128.2 and 129.3, corresponds to H_c protons, with $a_c = 0.9$ MHz. While the low-frequency ENDOR signal of H_a ($\nu - \nu_H < 0$), is positive, its high-frequency counterpart ($\nu - \nu_H > 0$) is negative with a smaller amplitude (ν_H is the proton Larmor frequency). The signals of H_b and H_c show a strong asymmetry as well. Upon increasing t_R the doublets intensities change significantly and the low- and high-frequency lines become of equal amplitudes, as expected for ^{1}H ENDOR spectra. This is demonstrated in Figs. 9b and 9c (the change in the noise levels of Figs. 9b and 9c is primarily a result of the smaller number of accumulations at each ENDOR frequency point). A similar but significantly smaller asymmetry was also observed for spectra recorded at $g_\perp$.

The electron spin–lattice relaxation time, T_{1e}, was estimated from the echo amplitude dependence on t_{mix} in Davies ENDOR sequence in the absence of the RF pulse (inversion-recovery experiment) (see Fig. 10a). This inversion-recovery curve provides the value of the baseline of the ENDOR spectrum for each mixing time, t_{mix}. Fitting this curve to an exponential function (solid line in Fig. 10a) gave a recovery time of 2.28 ± 0.07 ms, which is equal to T_{1e} when spectral diffusion can be neglected. In this plot the echo intensity at $t_{mix} = \infty$ was set to unity.

Figure 10b shows a series of ENDOR spectra recorded with $t_R = 10$ ms and different values of $t_{mix} < t_R$. These spectra are plotted on a common intensity scale, thus the position of the baseline of each spectrum corresponds to the echo amplitudes shown in Fig. 10a. When $t_{mix} > 3$ ms, asymmetries in the ENDOR spectra, similar to those discussed by Bennebroek and Schmidt (*4*) for $t_{mix} > T_{1e}$, are observed. The low-frequency line of H_a exhibits a negative ENDOR effect while its high-frequency partner has a positive effect. Interestingly, for $t_{mix} >$ 8 ms the intensity of the echo in the high-frequency ENDOR line region becomes larger than 1, which shows that the corresponding population difference at the moment of detection exceeds that predicted by the Boltzmann distribution.

The t_{mix} dependence of $F^{\alpha,\beta}_{ENDOR}$ of the H_a proton (126.8 and 130.7 MHz) in Cu-Imid is shown in Fig. 11. The data points were obtained by averaging the $F^{\alpha,\beta}_{ENDOR}$ values at the maxima of the H_a doublet in Fig. 10 over a bandwidth of 0.14 MHz. The solid lines present simulations with $T_{1e} = 2.28$ ms, $T_{1x} = 50$

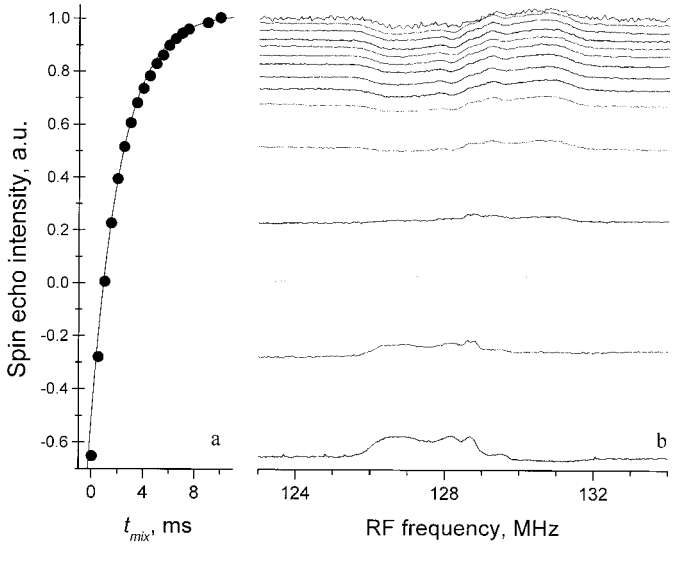

FIG. 10. (a) The dependence of the echo amplitude of Cu-Imid in an inversion recovery experiment. (b) The ENDOR spectra of Cu-Imid, recorded with different t_{mix}. Plots (a) and (b) have the same Y axis scale.

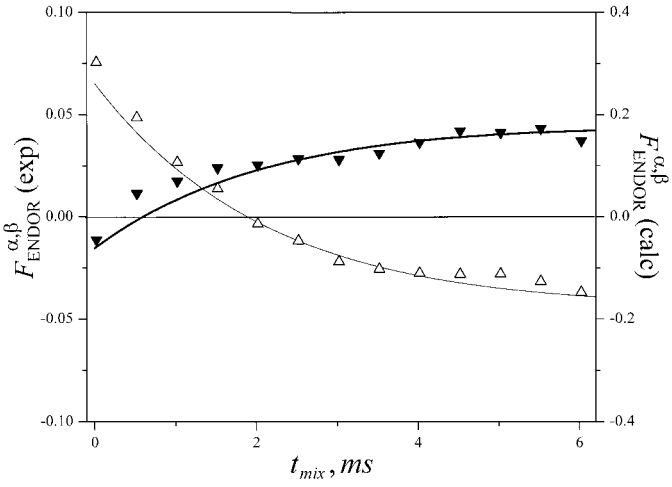

FIG. 11. Best fit of the experimental dependence of $F^{\alpha,\beta}_{\mathrm{ENDOR}}$ on t_{mix} of the doublet at 126.8 (open) and 130.6 MHz (solid symbols). The solid lines represent the calculated values obtained with $h\nu/kT = 0.83$, $t_{\mathrm{R}} = 10$ ms, $T_{1\mathrm{e}} = 2.28$ ms, $T_{1\mathrm{n}} = \infty$, $T_{1\mathrm{x}} = 50$ ms. Thin lines correspond to $F^{\alpha}_{\mathrm{ENDOR}}$ and thick lines to $F^{\beta}_{\mathrm{ENDOR}}$. The labels on the left and right axes represent the scale of experimental and calculated data, respectively.

ms, $T_{1\mathrm{n}} = \infty$, and $t_{\mathrm{R}} = 10$ ms, and the $F^{\alpha,\beta}_{\mathrm{ENDOR}}$ are given by the right-hand side ordinate. The difference between the experimental values of $F^{\alpha,\beta}_{\mathrm{ENDOR}}$ and those predicted by the theoretical model is attributed to inhomogeneous broadening and to the limited bandwidth of the pulses which were not taken into account in the model. While in the theoretical model the MW and RF pulses are considered ideal π and $\pi/2$ pulses, in the experiment the distribution of inversion pulse efficiencies, present due to the hole-burning nature of the experiment, leads to a reduced ENDOR efficiency. Nevertheless, this deviation affects only the amplitude of ENDOR effect and not its dependence on the various time intervals and relaxation rates. Therefore, the curves of the theoretical and experimental $F^{\alpha,\beta}_{\mathrm{ENDOR}}(t_{\mathrm{mix}})$ dependencies are presented using different scales, which is equivalent to the introduction of a normalizing factor accounting for deviation from the ideal conditions.

It was mentioned previously that for $h\nu/kT = 0.83$ it is possible to distinguish between nuclear and cross relaxation. In our experiments the comparison between the spectrum recorded with $t_{\mathrm{R}} = 100$ ms and simulations led us to favor the cross relaxation over nuclear relaxation.

DISCUSSION

The high-field ENDOR spectrum of the electronic system with $S = \frac{1}{2}$ coupled to a $I = \frac{1}{2}$ nucleus should, in general, have equal amplitudes for all lines. Nonetheless, the results presented here show that ENDOR spectra with asymmetric line amplitudes are expected at low temperature at two circumstances. When $T_{1\mathrm{n}}$, $T_{1\mathrm{x}} > t_{\mathrm{mix}} > T_{1\mathrm{e}}$, the ENDOR signals from the α manifold are negative and those of the β manifold are positive. The observation of such spectra is limited to very long mixing times (or RF pulses). This, however, does not represent optimal experimental conditions, where a high B_2 field and short RF pulses are preferred. The second case is more likely to be encountered experimentally because it does not require a very long mixing time and is a consequence of the saturation of the nuclear transitions. It occurs when $t_{\mathrm{mix}} < T_{1\mathrm{e}}$ and the cross- and/or nuclear-relaxation times are longer than t_{R} ($T_{1\mathrm{n}}$ or $T_{1\mathrm{x}} > t_{\mathrm{R}}$). In this case the polarization of the ENDOR signals becomes opposite of the previous case. Namely, the lines in the α manifolds are positive and those of the β manifold are negative. When $T_{1\mathrm{n}}$ and/or T_{x} ($1/\Gamma_{\mathrm{x}\uparrow}$ at very low temperatures) are of the same order of $T_{1\mathrm{e}}$, no asymmetry is encountered, because saturation does not occur. A sufficient polarization of the populations in different M_{S} manifolds is also an obligatory condition for the asymmetric ENDOR spectra observation.

The asymmetric ENDOR spectra allow direct determination of the sign of the hyperfine coupling. Hence, following the above analysis, one can choose experimental conditions that will lead to asymmetric doublets from which the sign can be determined. This may be useful in the analysis of various singularities in powder lineshapes. Moreover, by following the ENDOR effect dependence on the mixing time or the repetition rate it is possible to determine the various relaxation times. This, in turn, can be used to distinguish nuclei with different relaxation times or overlapping paramagnetic centers with different cross-relaxation times. The effect of the saturation of the nuclear transition can also result in the disappearance of signals of certain nuclei from the spectrum. For example, spectrum (b) in Fig. 9, which was recorded with a larger t_{R}, exhibits more features than spectrum (a). Although the theoretical model was developed for Davies ENDOR, it's extension to Mims ENDOR (*12*) is straightforward and similar results are expected.

Finally, we note that there have been a number of reports of continuous wave ENDOR spectra, recorded at Q-band frequencies and 2 K, which exhibited high asymmetries and negative ENDOR effect (*13*). We believe that this is again a consequence of the interplay between nuclear transitions at large thermal polarization.

CONCLUSIONS

Significant asymmetry in the amplitudes of ENDOR lines belonging to different M_{S} manifolds can be encountered under conditions of sufficient thermal polarization and the following circumstances: (i) when the nuclear- and cross-relaxation times are significantly longer than the electron spin-relaxation times and the echo is registered after a very long mixing time ($t_{\mathrm{mix}} \gg T_{1\mathrm{e}}$ and $T_{1\mathrm{n}}$, $T_{\mathrm{x}} \gg T_{1\mathrm{e}}$). In this case ENDOR signals from the α manifold are negative and those of the β manifold are positive; (ii) under conditions of short mixing times and saturation of the nuclear transitions. Namely, when the cross- and/or nuclear-relaxation times are longer than the repetition time ($t_{\mathrm{mix}} \ll T_{1\mathrm{e}} \ll t_{\mathrm{R}}$ and $T_{1\mathrm{n}}$, $T_{1\mathrm{x}} > t_{\mathrm{R}}$). In this case the polarization of the

ENDOR signals become opposite to the previous case, the lines in the α manifolds are positive, and those of the β manifold are negative. When T_{1n} and/or T_x are of the order of T_{1e} no asymmetries are encountered, because saturation does not occur.

APPENDIX

The characteristic relaxation rates in a four-level system are determined by the eigenvalues of the relaxation matrix Γ. The operator, $e^{-\Gamma t}$, describing the evolution of the populations, can be presented in the following form:

$$e^{-\Gamma t} = \sum_{i=1}^{4} \mathbf{V}_i^R e^{-\lambda_i t} (\mathbf{V}_i^L)^T, \qquad [20]$$

where the λ_i's are the eigenvalues and $\mathbf{V}_i^R$ and $\mathbf{V}_i^L$ represent, respectively, the right and left eigenvectors of Γ, defined as solutions of equations $\Gamma \mathbf{V}_i^R = \lambda_i \mathbf{V}_i^R$ and $\mathbf{V}_i^L \Gamma = \lambda_i \mathbf{V}_i^L$. An arbitrary state of the system can be presented as a superposition of eigenvectors, namely $\mathbf{n}(0) = \Sigma\, c_i \mathbf{V}_i^R$ with coefficients $c_i = (\mathbf{V}_i^L \cdot \mathbf{n}(0))$. Thus, the time dependence of $\mathbf{n}$ is given by

$$\mathbf{n}(t) = \left(\sum_{i=1}^{4} \mathbf{V}_i^R e^{-\lambda_i t} (\mathbf{V}_i^L)^T\right) \left(\sum_{i=1}^{4} c_i \mathbf{V}_i^R\right) = \sum_{i=1}^{4} c_i e^{-\lambda_i t} \mathbf{V}_i^R. \qquad [21]$$

Here we used Eq. [8] and the orthogonality condition for the eigenvectors, $(\mathbf{V}_i^L \cdot \mathbf{V}_j^R) = \delta_{ij}$. The $e^{-\lambda_i t}$ coefficients represent the time evolution of the individual contribution of each eigenvector.

The eigenvalues of Γ for the case $\Gamma_{x\uparrow} = \Gamma_{x\downarrow} = 0$ are

$$\lambda_1 = 0,\ \lambda_2 = 2\Gamma_n,\ \lambda_3 = \Gamma_\uparrow + \Gamma_\downarrow,\ \lambda_4 = \Gamma_\uparrow + \Gamma_\downarrow + 2\Gamma_n, \qquad [22]$$

or, using the definitions of relaxation times $T_{1n} = 1/(2\Gamma_n)$, $T_{1e} = 1/(\Gamma_\uparrow + \Gamma_\downarrow)$,

$$\lambda_1 = 0, \quad \lambda_2 = \frac{1}{T_{1n}}, \quad \lambda_3 = \frac{1}{T_{1e}}, \quad \lambda_4 = \frac{1}{T_{1e}} + \frac{1}{T_{1n}}. \qquad [23]$$

Taking into account that $\Gamma_\uparrow/\Gamma_\downarrow = \exp(-h\nu/kT)$, the eigenvectors in this case are

$$\mathbf{V}_1^R = \left(1, \exp\left(-\frac{h\nu}{kT}\right), 1, \exp\left(-\frac{h\nu}{kT}\right)\right),$$

$$\mathbf{V}_2^R = \left(1, \exp\left(-\frac{h\nu}{kT}\right), -1, -\exp\left(-\frac{h\nu}{kT}\right)\right),$$

$$\mathbf{V}_3^R = (-1, 1, -1, 1),$$

$$\mathbf{V}_4^R = (1, -1, -1, 1). \qquad [24]$$

The first eigenvector represents the Boltzmann equilibrium state and, as expected, its exponent $e^{-\lambda_1 t} = 1$. The second eigenvalue describes nuclear-spin relaxation whereas the third represents the electron-spin relaxation. The fourth eigenvector will contribute significantly only when the populations are concentrated on either levels 1 and 4 or 2 and 3. For example, such a situation occurs after a MW inversion pulse. In all other cases discussed in this work the c_4 coefficient in Eq. [21] is relatively small. Thus, a double-exponential decay with the characteristic times T_{1n} and T_{1e} is expected.

In the case of $\Gamma_n = 0$ and $\Gamma_x \neq 0$, the eigenvalues become

$$\lambda_1 = 0,$$

$$\lambda_2 = \tfrac{1}{2}(\Gamma_\uparrow + \Gamma_\downarrow + \Gamma_{x\uparrow} + \Gamma_{x\downarrow} - C),$$

$$\lambda_3 = \Gamma_\uparrow + \Gamma_\downarrow + \Gamma_{x\uparrow} + \Gamma_{x\downarrow},$$

$$\lambda_4 = \tfrac{1}{2}(\Gamma_\uparrow + \Gamma_\downarrow + \Gamma_{x\uparrow} + \Gamma_{x\downarrow} + C), \qquad [25]$$

where

$$C = \sqrt{(\Gamma_\uparrow + \Gamma_\downarrow + \Gamma_{x\uparrow} + \Gamma_{x\downarrow})^2 - 8(\Gamma_{x\uparrow}\Gamma_\downarrow + \Gamma_{x\downarrow}\Gamma_\uparrow)}. \qquad [26]$$

Under conditions of large thermal polarization $\Gamma_\uparrow/\Gamma_\downarrow = \Gamma_{x\uparrow}/\Gamma_{x\downarrow} \ll 1$ and the expressions for the eigenvalues in Eq. [25] can be simplified to

$$\lambda_1 = 0, \quad \lambda_2 = \frac{4 \exp\left(-\dfrac{h\nu}{kT}\right)}{T_{1e} + T_{1x}},$$

$$\lambda_3 = \frac{1}{T_{1e}} + \frac{1}{T_{1x}}, \quad \lambda_4 = \frac{1}{T_{1e}} + \frac{1}{T_{1x}}. \qquad [27]$$

Here again λ_1 corresponds to the Boltzmann equilibrium state and λ_3 represents the electron-spin relaxation and the corresponding eigenvectors are equal to $\mathbf{V}_1^R$ and $\mathbf{V}_3^R$ in Eq. [24]. The second and fourth eigenvalues represent complex relaxation processes and the respective eigenvectors are similar to the $\mathbf{V}_2^R$ and $\mathbf{V}_4^R$ of the previous case. In the expression for λ_2, the up and down components of the relaxation probabilities no longer appear as simple sums, making this relaxation rate temperature dependent. Under the condition of a fixed T_{1x}, the value of λ_2 will decrease exponentially with increasing temperature. It is this dependence that allows one to distinguish between the T_{1x} and T_{1n} contributions, as shown in Fig. 7.

ACKNOWLEDGMENTS

The authors thank M. G. Stepanov for fruitful discussions. This work was supported by the DFG Schwerpunkt program "High Field EPR in Physics, Chemistry and Biology."

REFERENCES

1. E. R. Davies, A new pulse ENDOR technique, *Phys. Lett.* **47A,** 1–2 (1974).
2. D. Goldfarb, K. G. Strohmaier, D. E. W. Vaughan, H. Thomann, O. Poluektov, and J. Schmidt, Studies of framework iron in zeolites by pulsed ENDOR at 95 GHz, *J. Am. Chem. Soc.* **118,** 4665–4671 (1996).
3. M. T. Bennebroek, A. Arnold, O. G. Poluektov, P. Baranov, and J. Schmidt, Shallow electron centers in silver halides, *Phys. Rev. B* **54,** 11276–11289 (1996).
4. M. T. Bennebroek and J. Schmidt, Pulsed ENDOR spectroscopy at large thermal spin polarizations and the absolute sign of the hyperfine interaction, *J. Magn. Reson.* **128,** 199–206 (1997).
5. P. Manikandan, B. Epel, and D. Goldfarb, Structure of copper(II)–histidine based complexes in frozen aqueous solutions as determined from high field pulsed ENDOR, *Inorg. Chem.,* in press, 2000.
6. C. Gemperle and A. Schweiger, Pulsed electron-nuclear double resonance methodology, *Chem. Rev.* **91,** 1481–1505 (1991).
7. H. Kurreck, B. Kirste, and W. Lubitz, "Electron Nuclear Double Resonance Spectroscopy of Radicals in Solution," Chap. 3, VCH, Weinheim, 1988.
8. A. Abragam, "The Principles of Nuclear Magnetism," Clarendon Press, Oxford, 1961.
9. H. Shikata, A phenomenological description of electron paramagnetic double-resonance relaxation of organic free radicals in solution. I. Theory of ENDOR based on the spin-population number method, *Bull. Chem. Soc. Japan* **50,** 3084–3089 (1977).
10. H. L. Van Camp, R. H. Sands, and J. A. Fee, Electron-nuclear double resonance on copper(II) tetra-imidazole, *J. Chem. Phys.* **75,** 2098–2107 (1981).
11. I. Gromov, V. Krymov, P. Manikandan, D. Arieli, and D. Goldfarb, A W-band pulsed ENDOR spectrometer: Setup and application to transition metal centers, *J. Magn. Reson.* **139,** 8–17 (1999).
12. W. B. Mims, Pulsed ENDOR experiments, *Proc. R. Soc. London A* **283,** 452–457 (1965).
13. J. Telser, Y.-C. Horng, D. F. Becker, B. M. Hoffman, and S. W. Ragsdale, On the assignment of nickel oxidation states of the Ox1, Ox2 forms of methyl-coenzyme M reductase, *J. Am. Chem. Soc.* **122,** 182–183 (2000).